AIAA 97-2325 15th AIAA Applied Aerodynamics Conference

WHOLE-FIELD VELOCITY MEASUREMENT IN UNSTEADY PERIODIC FLOWS

Reddy, U.C.†, Matos, C.A.†, Mahalingam, R.†, Komerath N.M.‡
School of Aerospace Engineering
Georgia Institute of Technology
Atlanta, GA 30332-0150

ABSTRACT

Measurements of the instantaneous and phase-resolved, ensemble-averaged velocity field in unsteady periodic rotorcraft flows are reported. A method is described for extracting the third component of velocity from 2-component planar velocity data in periodic incompressible flows, and is validated using numerical simulations. The differential mass conservation equation is used to solve for the third component using parallel slices of 2-D vector fields. A 2nd-order differencing procedure is shown to work even in the presence of 25% random noise added to simulate experimental data. The flowfield of a 2-bladed teetering rotor above a full-span 21% thick wing in low-speed forward flight in a wind tunnel is explored, with and without trailing edge flap deflection. A pulsed copper vapor laser sheet is used to illuminate the seeded flow. Flow image pairs from several chordwise planes are analyzed using Spatial Correlation Velocimetry (SCV) and resolved as a function of rotor azimuth. Ensemble-averaged velocity fields for discrete rotor azimuths are presented. Ensemble-averaged traces at selected points show the 1-per-rev variation caused by vortex interaction. The pressure data on the wing show the expected decrease in the time averaged pressure coefficient with flap deflection. Flap deflection is seen to cause substantial lateral deflection of the rotor wake, attributed to changes in the spanwise flow downstream of the unsteady 3D separation line. The efficient capture of the multidimensional velocity field is demonstrated in a large wind tunnel on a complex large-volume unsteady flow problem.

INTRODUCTION

The interaction between a rotor and a lifting surface is a basic problem in the development of rotary wing aircraft, especially tiltrotor aircraft. During the crucial phases of takeoff, transition and landing approach, the wake from the rotors flows down over the wings, with the strong vortices in the wake causing unsteady effects on the wings. The key to understanding the downloads, vibration, and their control lies in capturing the velocity field variation and pressure distribution in this complex flowfield. The extent of the vortical flowfield is large, in contrast to the traditional problems of streamlined aerodynamic configurations where the flow geometry is generally simple away from the boundary layer or thin shear layers. Traditional velocimetry using intrusive probes e.g. hot-wire and hot-film anemometry are inadequate to document the 3D flowfield with intermittent reversals. More recent laser-based non intrusive techniques such as Laser Doppler Velocimetry (LDV) and Particle Image Velocimetry (PIV) are now widely used in flow measurement. The former is a point wise technique whereas the latter is a planar technique. Point wise techniques are prohibitively expensive in facility run-time for such applications. The desire to overcome this limitation and get quantitative results from flow visualization data led to the development of planar velocimetry techniques that allow for the study of both steady and unsteady flows. PIV techniques are generally limited to small areas.

Until it becomes feasible to capture instantaneous whole-field volume-resolved velocity vector fields, scanning of multiple planes is a tractable alternative. The major problem is that the offset in time between planes constrains this technique to cases where identical flow events occur in repetitive runs, or the scanning can be done in so short a time that the velocity field can be assumed frozen for this duration. Since the rotor and rotor/body flows investigated at the authors' wind tunnel are periodic for the most part, measurement of multiple planes of two component velocity fields using a correlation method (described below) is used here as a precursor to the complete 3D three component velocity field measurement. The latter is demonstrated computationally by using the fact that the flowfield is incompressible.

PREVIOUS WORK

In PIV techniques [1] - [4], the displacement between peaks of the spatial autocorrelation of double-pulsed images is computed over small particle image areas, with the sign of the displacement vector determined through additional instrumentation such as rotating mirrors, color or polarization differences between the two laser pulses, etc. Alternately, fringe patterns formed by passing laser beams through double-exposed image transparencies are digitized. PIV techniques generally require powerful double-pulsed lasers and high-resolution optics in addition to extensive post-processing and computation. They remain confined to small areas by the need to use seed particles which are small enough to follow the flow while being large enough so that their scattering can be resolved, but they provide high accuracy and temporal resolution. As late as 1986, full cross-correlation

between two images was declared impractical for planar velocimetry in flows[4]. Direct cross-correlation for planar velocitmetry was first shown in Ref. 5. Since then, some PIV implementations have appeared (Ref. 6 and 7, for example) where direct cross-correlation is performed, but they remain limited to small areas by the need to resolve particle images. We use the method shown in Ref. 5, applied to large areas.

Meng and Hussain [8] used Holographic Particle Velocimetry (HPV) where 3D information is recorded instantaneously from a well seeded flow. Autocorrelation was used for double-exposed holograms, each hologram being reconstructed separately. Cross-correlation was used for single-exposure holograms, requiring two holograms that are recorded at different instants in the same time series. However both these operations were performed as 2D operations giving only two velocity components. They proposed an orthogonal view of the recording supplying the third component. This is somewhat redundant since the 3D information is already recorded within one view but is often difficult to extract. Huang, Slepicka and Cha [9] developed Holographic Diffraction Image Velocimetry (HDIV) which can measure 3D three component velocity fields. They used off-axis holography where multiple scenes can be separately recorded on a single holographic plate and then independently reconstructed, by employing an individual reference beam for each scene. HDIV processing is rather involved, including holographic recording, image calibration and 3D image correlation.

Recently, the Doppler Global Velocimetry technique [10] has shown great promise in some applications. DGV is a non-intrusive, global, three-component velocity measurement technique. This technique was used to measure steady state velocities of the flow on the inlet side of the tail rotor fan of a 15% scale helicopter by Gorton [11]. LV measurements were also made for comparison. Three pairs of cameras (a signal camera and a reference camera) were used, one pair for each velocity component. Smoke particles injected into the flow scattered light with a Doppler-shift in proportional to the particle velocity. Normalization of the signal image by the reference image removes spatial variations in smoke density, particle size distributions and non-uniformities in the light sheet. However, resolution of Doppler shift requires laser illumination, a set of 4 to 6 cameras, and poses scale-up and resolution problems at the large-size / low speed end of the velocity spectrum.

Over the past decade, we have developed Spatial Correlation Velocimetry (SCV), where the statistical properties of "clouds" of inhomogeneities are directly used in determining the flow velocity. This is a superset of the particle image velocimetry techniques, and reduces to digital cross-correlation PIV in small areas where particle images can be resolved However, our focus has been on the large rotorcraft flowfields where single-particle resolution would requires prohibitively-expensive optics, illumination systems and post-processing systems. Transformation to the frequency domain enables efficient computation of the multi-dimensional cross-correlation. SCV has been demonstrated on both steady and unsteady configurations. Ref. [12] outlines the technique and gives several demonstrations. Fawcett and Komerath [13] applied the technique to low speed flow over a wing at a steady angle of attack and then to the same wing executing large amplitude plunging motion, with intermittent flow reversal. Extraction of time-sequences of velocity at a point in this flow, and the use of moving-window averaging, were demonstrated. Ref. [14] described measurements over a continuously changing wing/ canard configuration, thus demonstrating application to quasi steady aerodynamic testing in a 7' x 9' wind tunnel. Instantaneous velocity profiles were measured in the canard-wing interaction flowfield. SCV has also been applied to more complex, completely three-dimensional rotor flows. Funk, Fawcett and Komerath [15] measured the wake of an isolated rotor in forward flight using SCV, showing robustness of the technique in flows where the out-of-plane velocity component is substantial.

SPATIAL CORRELATION VELOCIMETRY

The basic premise in SCV is that most of the energy of the flow is contained in larger "packets" or eddies of fluid. If adequate seeding exists in all parts of the image, this method gives an instantaneous picture of velocities in the imaged plane. In the larger area case, it is difficult to keep seeding in all areas at all times. An intensity criterion is then used to validate the computed vectors. If the average intensity of a sub-image area surpasses a user defined threshold it is assumed that adequate seeding levels exist in the sub-image area and the vector is valid. Another criterion used to eliminate unreliable vectors is the ratio of the second largest and largest peaks in the cross-correlation function. If the ratio exceeds a threshold value then there are two equally probable values for velocity at the same point. Therefore neither of them can be reliable.

Moving window averaging enables a large improvement in the statistical accuracy of the vector computed. The subimage origin is successively moved by 8 pixels in each iteration. All vectors in a given area are then averaged to obtain a more stable vector plot. The 3577 vectors computer per image pair are averaged down to about 300 for convenience of storage and presentation. Another useful technique is ensemble averaging which compensates for lack of seeding in some areas by averaging corresponding vectors in several images at the same azimuth (for periodic flows).

THIRD VELOCITY COMPONENT SOLVER

Since our primary interest is in low-speed air flows where density does not vary, we compute the third velocity component by satisfying the continuity equation. A second order TVC (Third Velocity Component) solver has been developed. The solver steps across the flow, starting from two boundary planes where the component of velocity normal to the plane is known (usually zero or constant), so that all components and their gradients can be specified in these planes. In the wind tunnel this is done simply by going away from the rotor wake region and, where necessary, going near the tunnel walls.

Analytical test case

A test case of rotating flow interacting with ground was chosen to validate the TVC algorithm. This problem is one of the few 3D flows with an exact solution to the Navier-Stokes equation. It was chosen because the flow contains some of the elements of a helicopter ground effect flow, though the axial flow is in the opposite direction. Also missing are the strong tip vortices. However, we do have a swirling flow, a rapidly varying axial velocity profile and a large radial variation near the ground plane. Fluid at large distances from the ground is in equilibrium under the influence of centrifugal force and radial pressure gradient and is assumed to rotate like a rigid body. In the boundary layer, viscous forces attenuate the outward centrifugal force and there is a radial inflow as shown in Fig. 1. The secondary flow upwards ensures that continuity is satisfied. The Navier-Stokes equations in cylindrical coordinates are used. The boundary conditions are:

$$z=0;\ u=0;\ v=0;\ w=0 \quad \text{and} \quad z=\infty;\ u=0;\ v=r\omega$$

where u, v and w are, respectively, the radial, tangential and axial components of velocity. At large distances from the ground the flow is rotating at a constant angular velocity of ω. Introducing the dimensionless coordinate $\zeta = z\sqrt{\frac{\omega}{\nu}}$ and assuming that the velocity components have the form: $u = r\omega\, F(\zeta)\ ;\ v = r\omega\, G(\zeta)\ ;\ w = \sqrt{\nu\omega}\, H(\zeta)$, we obtain a system of ordinary differential equations given below.

$$\begin{aligned} F^2 - G^2 + HF' - F'' + 1 &= 0 \\ 2GF + HG' - G'' &= 0 \\ 2F + H' &= 0 \end{aligned} \qquad (1)$$

with the boundary conditions:

$\zeta = 0 : F = 0;\ G = 0;\ H = 0$

$\zeta = \infty : F = 0;\ G = 1$

This system of equations was first solved by U.T. Bödewadt[16] in a very laborious way by means of a power series expansion. This was corrected by J.E. Nydahl[17] and it is his solution tabulated in Schlichting[18] that has been used to generate the desired velocity field. The axial velocity component depends only on the distance from the ground.

A Cartesian coordinate system is chosen here so that the code is not restricted to axially symmetric flows. A second order difference scheme is used to discretize the continuity equation -- central difference at all interior points and one sided difference at the boundaries. The third component was calculated using a backward difference scheme. A second order scheme requires two boundary planes.

Implementation

The solution from Schlichting[18] was used to generate 27 slices of 2D velocity data (a 41 x 31 grid of radial and azimuthal velocity components) parallel to the ground. The 3D vector field obtained from this solution in two planes parallel to the ground is shown in Fig. 2. For testing the TVC solver two components were taken from the known solution and the third was computed. The farfield angular velocity specified was 1050 RPM. The distances are non-dimensionalized by the square root of the ratio of kinematic viscosity to the farfield angular velocity. The non-dimensional factor for the axial velocity component is the square root of their product. The radial and tangential components are non-dimensionalized by the angular velocity in the farfield at the same radial station. For this flow, the axial velocity (perpendicular to the ground) varies only with distance from the ground. Hence the plots shown for the reconstructed axial velocity are one dimensional - the x-axis being height from the ground and the y-axis being the axial velocity averaged at all grid points at the same height. The non-dimensionalized radial and tangential components are also functions of only distance from the ground. The procedure is further described in [19].

Boundary Conditions

Exact and calculated values of the axial velocity component at varying distances from the ground is shown in Fig. 3. The solid line denotes the solution obtained by numerically solving the Navier-Stokes equations. The dotted line is the axial velocity profile obtained using a second order finite difference scheme with two boundary planes specified. Fig. 3(a) shows the comparison with two boundary planes specified at the ground.

When the two boundary planes are chosen in the farfield, there is a very good match with the exact solution except for a small region near the ground where the gradient in the axial velocity profile is steep as seen in Fig. 3(b). Therefore better reconstructions are obtained by specifying boundary conditions in regions of relatively low gradient in the third component. In order to check the applicability of the method to the reconstruction of any component of the flow the radial and tangential velocities were also reconstructed from

2D data planes of the other two components. A comparison of the exact and calculated profiles is shown in Fig. 4.

Addition of random noise

In the earlier comparisons the two inplane components used were exact values. To simulate experimental data, random noise upto 25% of the exact values was added to the radial and tangential components. It was found that the resulting axial velocity profile closely matches the zero noise case.

Adding as much as 25% random measurement noise to the data still gives good reconstruction for both the nearfield (Fig. 5) as well as farfield boundary cases. This is a conservative level of accuracy for experimental data even without phase averaging. The SCV technique itself is quite robust to experimental noise.

Interpolation

When experimental data are used with the TVC solver, interpolation routines become a necessity. In regions where data are not available or not reliable, in-plane velocities can be interpolated. The computation of the third component involves computing gradients from velocity values at surrounding grid points. Interpolation is also required between planes to increase the resolution of the 2D velocity data in parallel planes. A second order interpolation scheme is required since a first order scheme would only enhance the error in the second order finite difference scheme being used. Second order polynomial interpolation was chosen as the most suitable.

FLOW EXPERIMENT

Set-up:

The experimental set-up in the 2.7 m x 2.5 m test section of the John J. Harper windtunnel at Georgia Tech. is shown in Fig. 6. It consists of a full-span NACA0021 wing with 400 mm chord at a 0° angle of attack to the freestream direction. It is mounted on a stand below a 914 mm diameter, two-bladed teetering rotor. The rotor is mounted on the tunnel roof with its hub at 127 mm upstream of the wing leading edge and centered at mid-span A cambered flap with a 125 mm chord is attached to the trailing edge of the wing. The maximum flap deflection achievable is 27 degrees.

The rotor was run at 1050 RPM and an advance ratio of 0.075 was maintained by keeping the tunnel freestream steady at 3.77m/s. A dual-camera system is setup on a traverse outside the test section, with the shutter of one camera delayed by a specified interval with respect to the shutter of the other. With a pulsed copper vapor laser source operating at 5994 pulses/sec, test parameters are adjusted to give one laser pulse per image. A third camera is used to keep track of the rotor azimuth by focusing on the azimuth disk attached to the rotor shaft. The light sheet optics are set up on a traverse located 2.54 m downstream of the rotor hub. Smoke generators used to seed the flow are located 2.54 m upstream of the rotor hub.

Procedure:

The optics stand traverse downstream of the wing is first moved such that the vertical laser light sheet is on the desired chordwise plane. A 55 cm X 40cm gridboard is placed vertically in this plane covering much of the image area of interest during the camera calibration. The smoke outlet is positioned by trial and error so that smoke enters the light sheet. The measurement area is about 65cm x 50cm between the rotor and the wing extending from the rotor hub to beyond the flap hinge at the wing TE. Two flap settings were tested - zero and 27° flap deflection. The angle of attack of the wing is verified to be 0°for each run. The two cameras are aligned to within 1 pixel error. The gridboard view is recorded for use in removing distortion error.

At the test condition of 1050RPM rotor speed and 3.77m/s tunnel speed, the smoke is turned on and flow visualization recorded. This is repeated for 3 different delays between the camera shutters to capture a wider range of flow speeds. The faster the flow the smaller the delay needed. Typically, delays are of the order of a few milliseconds. The light sheet is stepped normal to itself in steps of 5cm covering the entire rotor wake and extending to the tunnel wall on the retreating blade side. Several images are captured at each location for phase averaging. Since the frame rate is 30 frames/sec. and half frames are also used, each second of video recording yields 60 different images of the flow. Note that the delay between camera shutters is the temporal resolution of the velocity measurement.

Data Reduction:

The recordings from the two cameras are digitized as movies of about 10sec. duration, and analyzed, one image pair at a time. The rotor azimuth is determined from the display of the azimuth disk that is mixed in with one of the video signals. Images are sorted according to azimuth and all vector fields at the same azimuth are averaged to get the phase averaged results. For a rotor RPM of 1050 the azimuth cycle consists of 24 discrete azimuths after which they repeat (since each subsequent frame is 1/60 sec, apart during which time the azimuth changes by 105°). A total of 600 vector fields were obtained at each chordwise station in the flow. These were then averaged into the 24 azimuth bins, so that 25 vector fields were ensemble averaged in each bin. The vector fields thus obtained are not strictly instantaneous, but are associated with the middle of the delay between the two shutters.

Run times

The experiments described in this paper were conducted in a total tunnel occupancy time of less than 4 weeks. The tunnel was run on 10 days. The SCV data acquisition runs was completed in 6 days. This compares with about 2 months needed to complete 2

component LDV measurements in one chordwise plane for a similar configuration, reported in Ref. 20.

RESULTS

Steady pressure

The mean pressures were measured using static ports on the wing, multiplexed through a scanivalve to a barocel output. The pressures were referenced to freestream dynamic pressure. Fig. 7 compares the pressure coefficient with 0 and 27° flap deflection along a the chord at y/R = 0.03. Figs. 8(a) and 8(b) show the mean pressure coefficient on the top surface of the wing under the Retreating Blade Side (RBS) of the rotor. The effect of rotor-wake impingement includes a large region of positive pressure, with Cp's above 2, due to the stagnation pressure in the wake being higher than in the tunnel freestream. The positive pressure region is greatly reduced when the flap is deflected 27° as seen in Fig. 8(b)., with the maximum Cp reaching about 1.0.

Effect of flap deflection

The pressure measurements with the flap deflected show a decrease of mean pressures throughout the wing surface as expected. The surface pressure reduction corresponds to a ΔCp of 1.4. The spatial extent of the download reduction is clearly seen in the pressure contours (Fig. 8) near the rotor hub region. Velocity field at the mid-span plane (y/R=0) was obtained for both flap deflection cases. One such pair at a rotor azimuth of 324° is shown in Fig. 9. The velocity field with flap shows a clear downward deflection of the flow near the flap hinge at the wing trailing edge. This is expected as the positive flap deflection must induce a downflow unless there is flow separation. Also, for this particular azimuth the reversed flow due to vortex impingement is seen to occur further downstream of the wing leading edge when the flap is deflected.

The surprising result however, was the overall reduction of velocity magnitudes in the flap deflected case. A possible explanation for this is the decrease in the spanwise flow on the wing surface. It was shown in Refs. [20] and [21] that there is a strong spanwise flow directed towards the RBS downstream of the 3-D separation line formed on the wing during vortex interaction. By deflecting the flap and allowing the flow to deflect downstream this spanwise flow is reduced. This suggests that the rotor wake is skewed towards the Advancing Blade Side (ABS) when compared to the flap undeflected case. Thus the velocity field at y/R=0 plane with flap deflection actually corresponds to that at a chordwise plane shifted towards RBS when flap is undeflected. This explains the lower velocities measured in the mid-span plane with flap deflection.

Velocity field

The downstream half of the rotor wake region between the tip path plane and the wing surface was measured. The wing of a tiltrotor corresponds to the RBS of the present configuration. Fig. 10 shows the azimuthal variation of the ensemble averaged streamwise and vertical velocity components at a point 10.16cm downstream of the hub and 12.7cm above the wing centerline. The once-per-revolution variation is expected [20]: due to vortex interactions the flow pattern at a given point repeats only once per revolution. The variation is quite consistent, even though the individual values are picked off different vector fields. However, there is more scatter from point to point than we see in ensemble-averaged LDV data [20]: this is not surprising, given that only 25 values are averaged in each azimuth interval. compared to an average of 300 points in a typical LDV azimuthal bin.

Figures 11 and 12 show the 2D ensemble-averaged velocity field overlaid on vorticity contours at several RBS chordwise vertical planes. At the y/R=0 plane shown in Fig. 9a, the flow is predominantly in the freestream direction with velocity magnitudes of about 3 to 4 m/s (freestream is 3.77m/s). Velocity and vorticity fields at 4 planes 10.16cm apart are shown in Fig. 11 at rotor azimuth Ψ = 174 deg. to illustrate the spatial variation of the flowfield. Similar data are shown in Fig. 12 at Ψ = 324 deg. The reversed flow region due to vortex interaction near wing leading edge is more visible away from the y/R=0 plane for the azimuths shown. This corresponds to the negative vorticity seen developing near the leading edge. Regions of comparable vorticity are also seen upstream of the trailing edge for the 324° azimuth case (Fig. 12). This indicates two vortex trails impinging on the wing - one that goes over the leading edge and the other that goes over the wing surface.

The effect of the first vortex trail on the velocity field is seen by comparing Fig. 12(c) and (d). The two planes are 30.5cm and 40.6cm from the mid-span location respectively (on RBS). In Fig. 12(c) the flow above X/R = 0.4 is seen to diverge with one branch flowing upstream and the other downstream. In Fig. 12(d) the first vortex appears to have just disappeared below the leading edge and the local upflow due to its clockwise rotation is clearly seen.

The variation with azimuth at a given station is seen by comparing velocities in the y/R=0 plane (Figs. 11(a) and 12(a)). The flowfield feature appears to have moved by 0.2R (9.144cm) from azimuth 174° to 324° ie. a range of 150°. This azimuth range is covered by the rotor in 23.81 ms which gives a translation speed of 3.84m/s between the two images. This closely matches the freestream speed of 3.77m/s, thus confirming the azimuthal variation seen in the two images.

CONCLUSIONS

This work presents a capability to quantify instantaneous 3D velocity fields over large volumes in unsteady, incompressible periodic flows. Several conclusions are made:

1. We have shown that the extension of the planar SCV technique to three dimensions is possible using several closely spaced parallel planes of 2D velocity data. A second order finite difference scheme with two boundary planes specified is sufficient for a reliable reconstruction of the third velocity component.
2. The robustness of the TVC solver to random experimental noise has been demonstrated.
3. The SCV technique has been successfully used to generate phase-resolved, ensemble-averaged velocity fields in a 3D periodic rotor wake over a wing.
4. Ensemble-averaged velocity values at a selected location show the expected once-pre-rev variation seen in previous LDV data. The consistency of the data is encouraging despite the very small number of points averaged in each azimuthal bin.
5. The planar velocity data are consistent enough to compute vorticity contours which show the expected flow features. The divergence of the vortex trajectories, and their flowfield effects, are clearly seen.
6. The convection speed of these features matches the freestream component of velocity.
7. Pressure measurements on the rotor-wing configuration show a marked decrease in pressure coefficient due to flap deflection.
8. The velocity field change due to flap deflection indicates a spanwise shift in the wake, attributed to a decrease in spanwise velocity.
9. These measurements demonstrate that velocity fields in large-scale rotorcraft interaction flowfields can be efficiently quantified using the Spatial Correlation Velocimetry technique.

ACKNOWLEDGMENTS

This work was performed under Task RUA-2 of the Center of Excellence Augmentation Grant, funded by the Army Research Office, and under the NASA/Army Rotorcraft Center of Excellence. The technical monitors are Mr. John Davis and Dr. T.L. Doligalski.

REFERENCES

1. R.J. Adrian, "Image Shifting Technique to Resolve Directional Ambiguity in Double-Pulsed Velocimetry", Applied Optics, 25,. 21, pp. 3855-3858, Nov. 1986.
2. Adrian, R.J., Yao, C-S., "Method and Apparatus for Measuring the Displacements of Particle Images for Multiple Exposure Velocimetry". United States Patent 4,729,109, March 1988.
3. Adrian, R., "Strategies for Imaging Flowfields", AIAA-96-1988, June 1996.
4. Smith, C.A., Lourenco, L.M.M., Krothapalli, A., "The Development of Laser Speckle Velocimetry for the Measurement of Vortical Flow Fields". AIAA 86-0763, March 1986.
5. Komerath, N.M., *Fawcett, P.A.*, Ballarini, D., "Planar Velocimetry Using Digital Cross-Correlations". Developments in Theoretical and Applied Mechanics. Vol. XV, March 1990, p. 471 - 478.
6. Willert, C.E., Gharib, M., "Digital Particle Image Velocimetry". Experiments in Fluids, 10, 181-193, 1991.
7. Utami, T., Blackwelder, R.F., "A cross-correlation technique for velocity field extraction from particulate visualization". Experiments in Fluids, 10, 213-223, 1991.
8. Meng and Hussain, 'Holographic particle velocimetry: a 3D measurement technique for vortex interactions, coherent structures and turbulence,' Fluid dynamics research, Vol.8, 1991.
9. Huang, Slepicka and Cha, 'Cross-correlation of three-dimensional images for three-dimensional three-component fluid velocity measurements,' SPIE, Vol. 2005, 1993.
10. Komine, H., Brosnan, S.J., Litton, A., Stappaerts, E.A., "Real Time, Doppler Global Velocimetry". AIAA 91-0337, January 1991.
11. Gorton, S.A., Meyers, J.F., Berry, J.D.,"Velocity Measurements Near the Empennage of a Small-Scale Helicopter Model", AHS 52nd Annual Forum, Washington, D.C., June 1996.
12. Komerath, N.M., Fawcett, P.A., "Spatial Cross-Correlation Velocimeter", United States Patent No. 5,249,238, Sept. 1993.
13. Fawcett, P., Komerath, N.M., "Spatial Correlation Velocimetry in Unsteady Flows", AIAA 91-0271, Jan. 91.
14. Fawcett, P.A., Funk, R.B., Komerath, N.M., "Quantification of Canard and Wing Interactions Using Spatial Correlation Velocimetry", AIAA 92-2687, 10th Applied Aerodynamics Conference, Palo Alto, CA, June 1992.
15. Funk, R.B., Fawcett, P.A., Komerath, N.M., "SCV Measurements in the Wake of a Rotor in Hover and Forward Flight", AIAA paper 93-3080, 24th Fluid Dynamics Conference, Orlando, FL, July 1993.
16. Bödewadt, U.T., Die Drehströmung über festem Grund. ZAMM 20, 241-253 (1940).
17. Nydahl, J.E., "Heat transfer for the Bodewadt problem", PhD Thesis, Colorado State University, Fort Collins, Colorado, 1971.
18. Schlichting, H., 'Boundary Layer Theory', McGraw-Hill Book Company, Seventh edition.
19. Komerath N.M., Fawcett, P.A., Funk, R.B., Reddy, U.C., "Large-Area Velocity Measurement in Low-Speed Flows", ICIASF, July 1995.
20. Funk, R.B., Komerath, N.M., "Proceedings of the 51st Annual AHS Forum and Technology Display", Fort Worth, TX, May 1995.
21. Foley, S.M., Funk, R.B., Fawcett, P.A., and Komerath, N.M., "Rotor Wake-Induced Flow Separation on a Lifting Surface", Journal of the American Helicopter Society, Vol.40, No.2, April 1995.

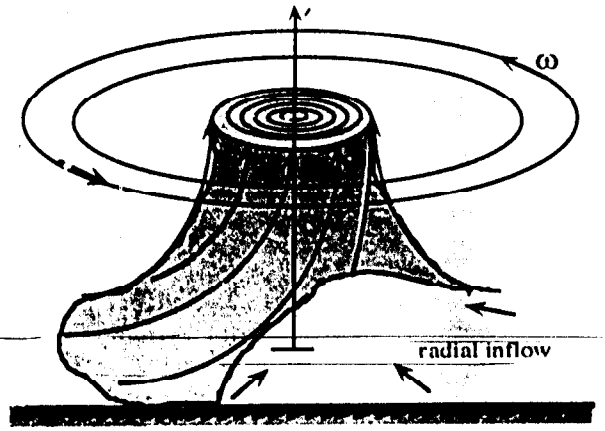

Fig 1: Schematic for rotation of flow near the ground

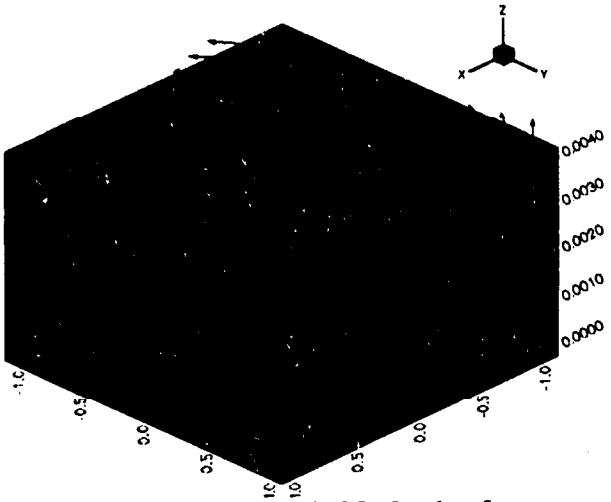

Fig. 2: The 3D velocity field obtained from Navier Stokes solution

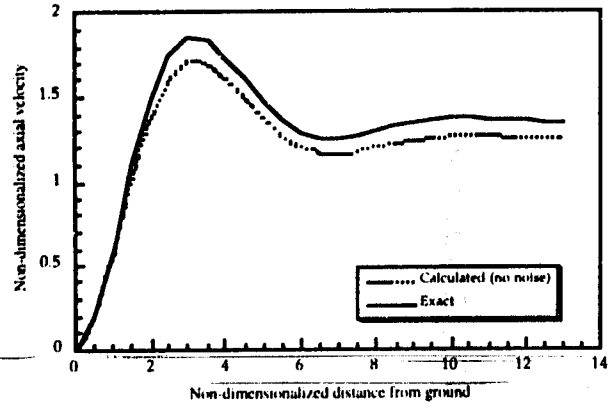

Fig. 3(a): Axial velocity profile with ground boundary planes.

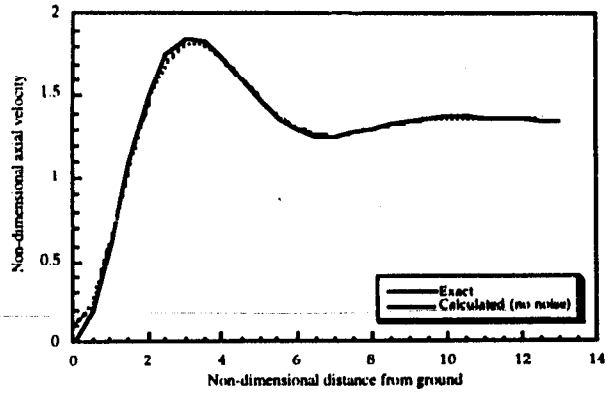

Fig. 3(b): Axial velocity profile with farfield boundary planes.

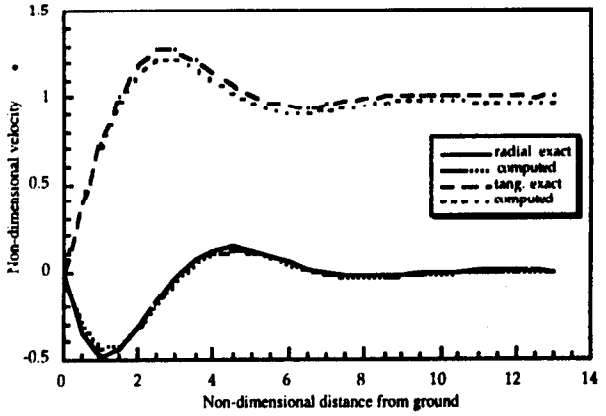

Fig. 4: Radial and Tangential velocity profiles

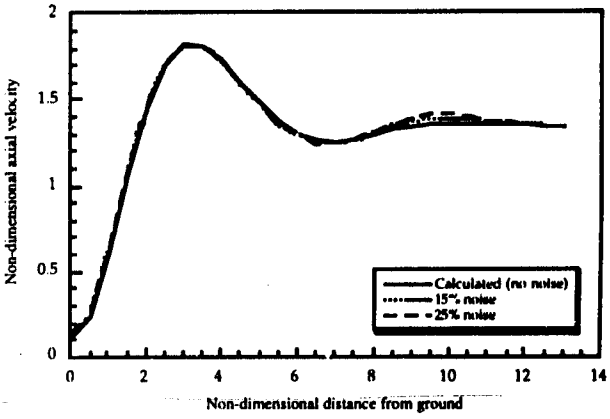

Fig. 5: Modelling experimental error (with ground boundary planes)

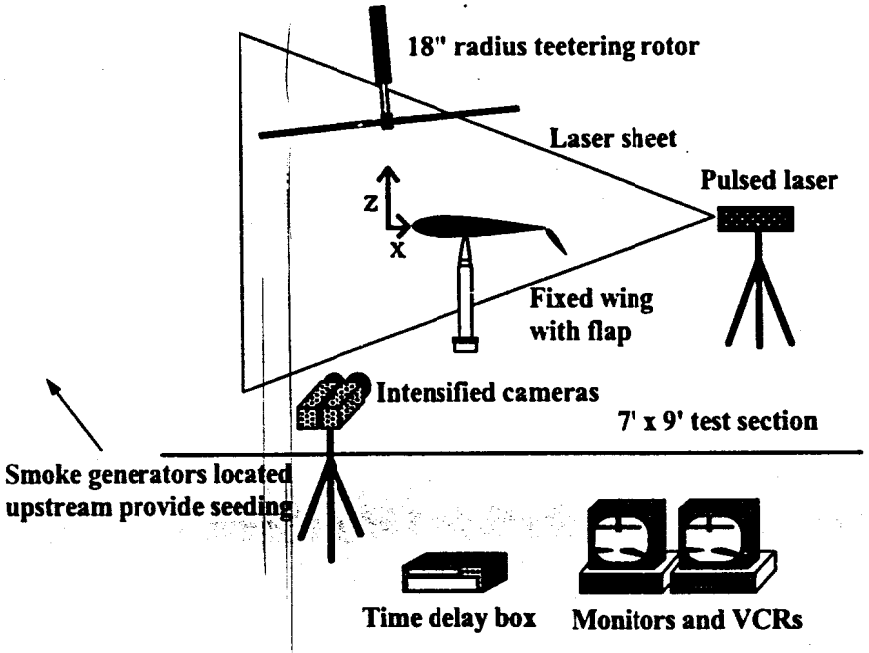

Fig. 6: Experimental Setup

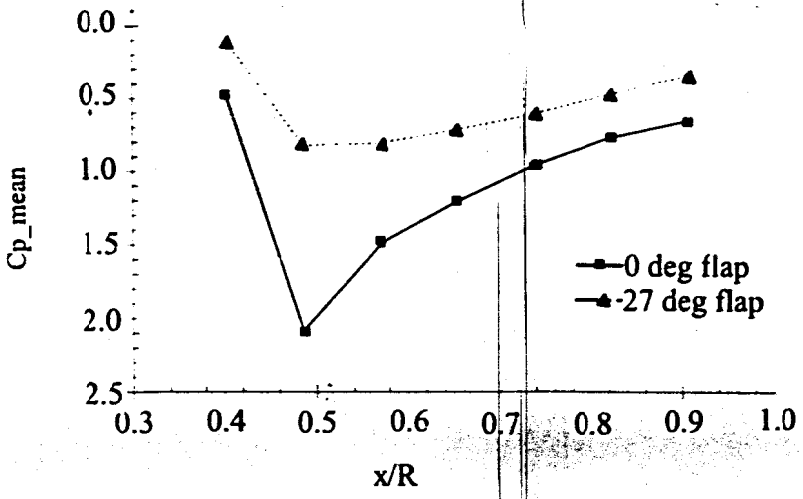

Fig. 7: Chordwise distribution of mean Cp at y/R=0.03 [Wing LE at 0.28, TE at 1.43]

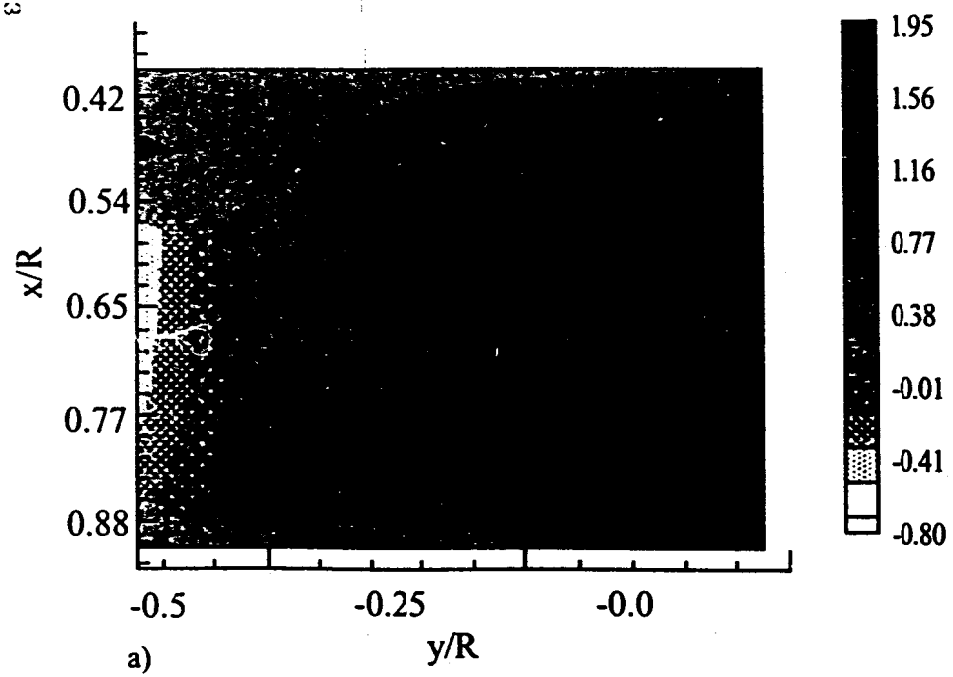

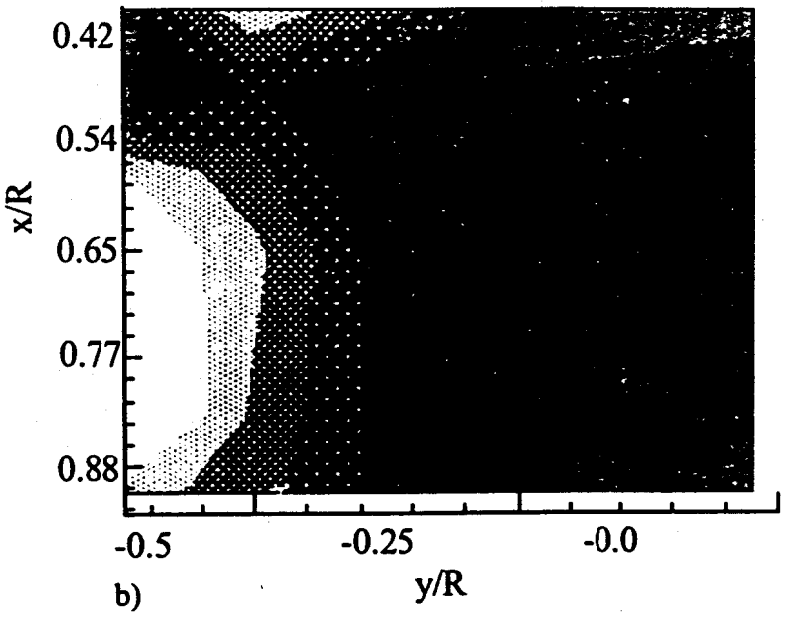

Fig. 8: Surface pressure contours a) flap deflection 0 degrees, b) flap deflection 27 degrees

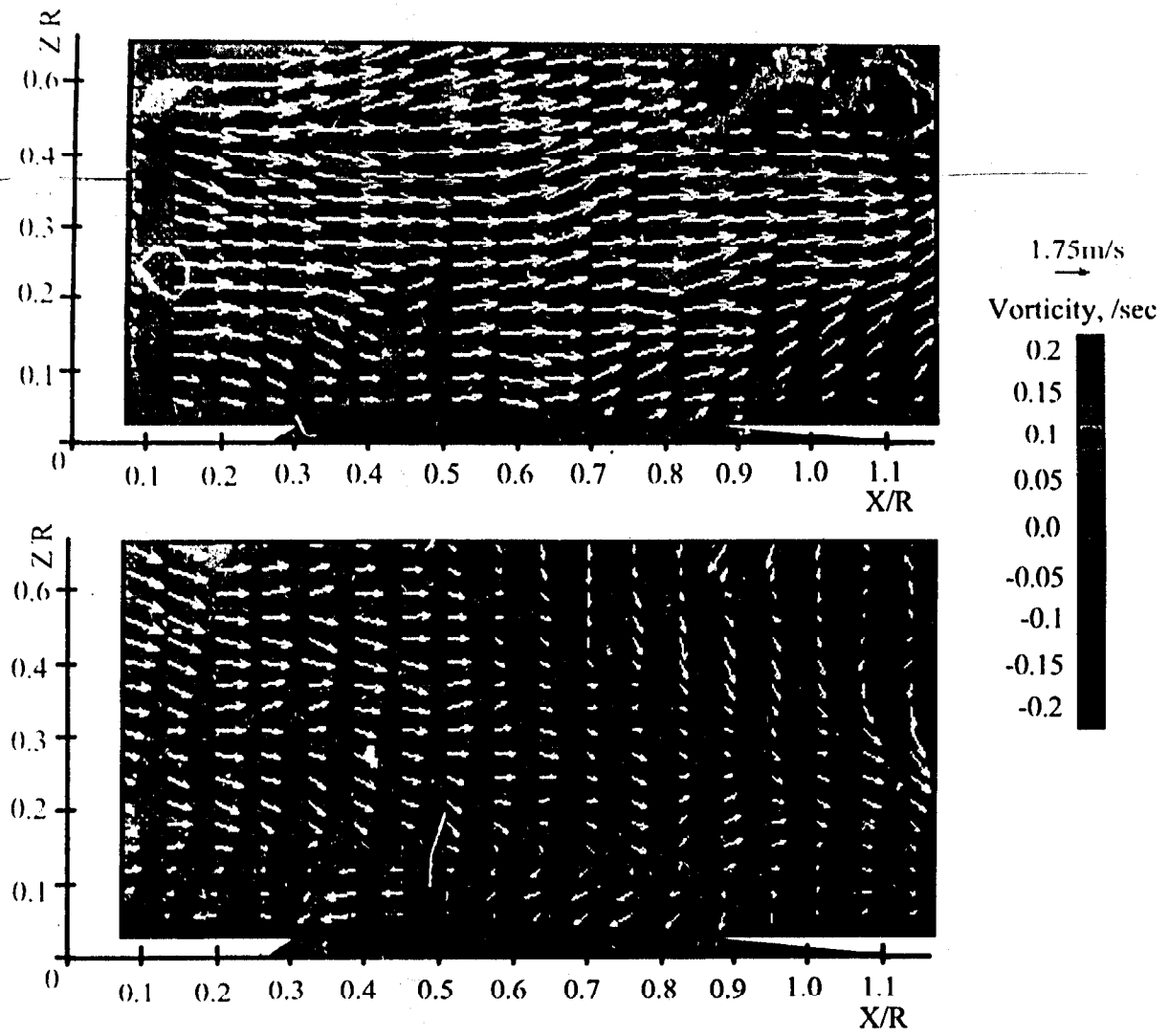

Fig. 9. Planar Vorticity and velocity along the center-line of the wing, Ψ ~ 324
a) flap at 0 degrees, b) flap at 27 degrees

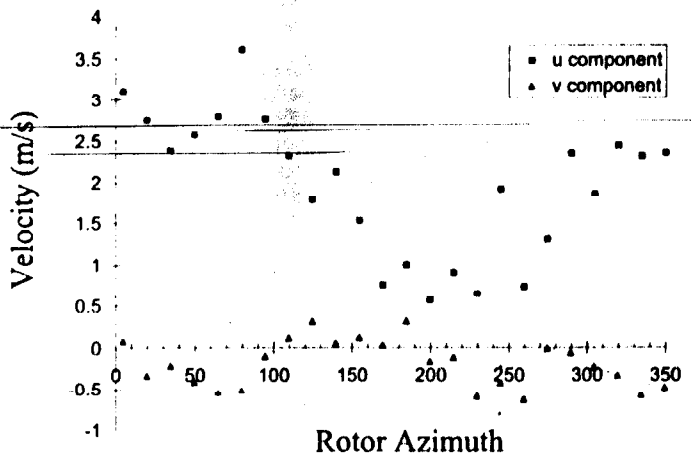

Fig. 10: Azimuth averaged velocity components in the y/R=0 plane with zero flap deflection
X/R = 0.22, Z/R = 0.28

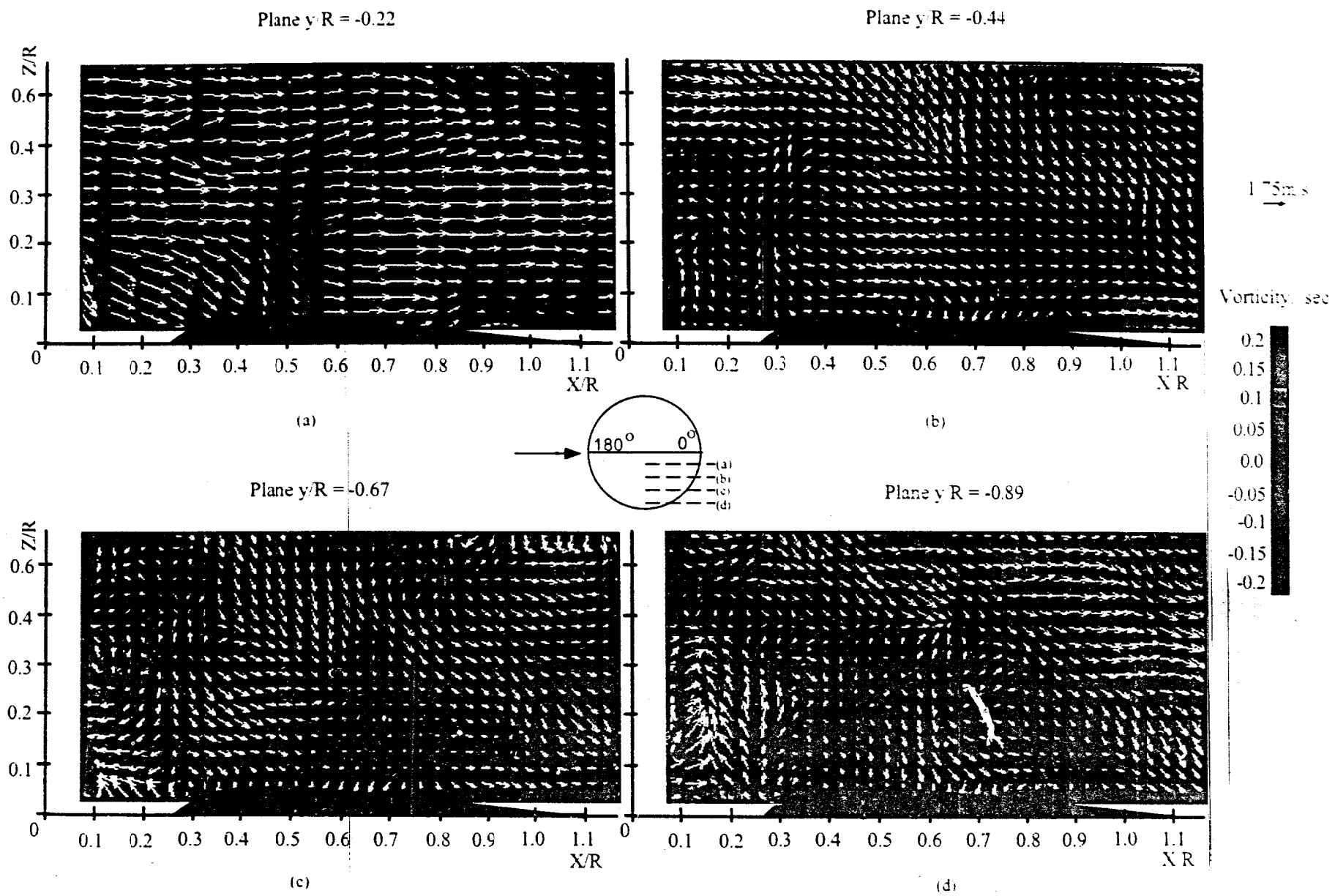

Fig. 11. Velocity vectors and vorticity contours for chordwise planes on the RBS, Ψ ~ 174

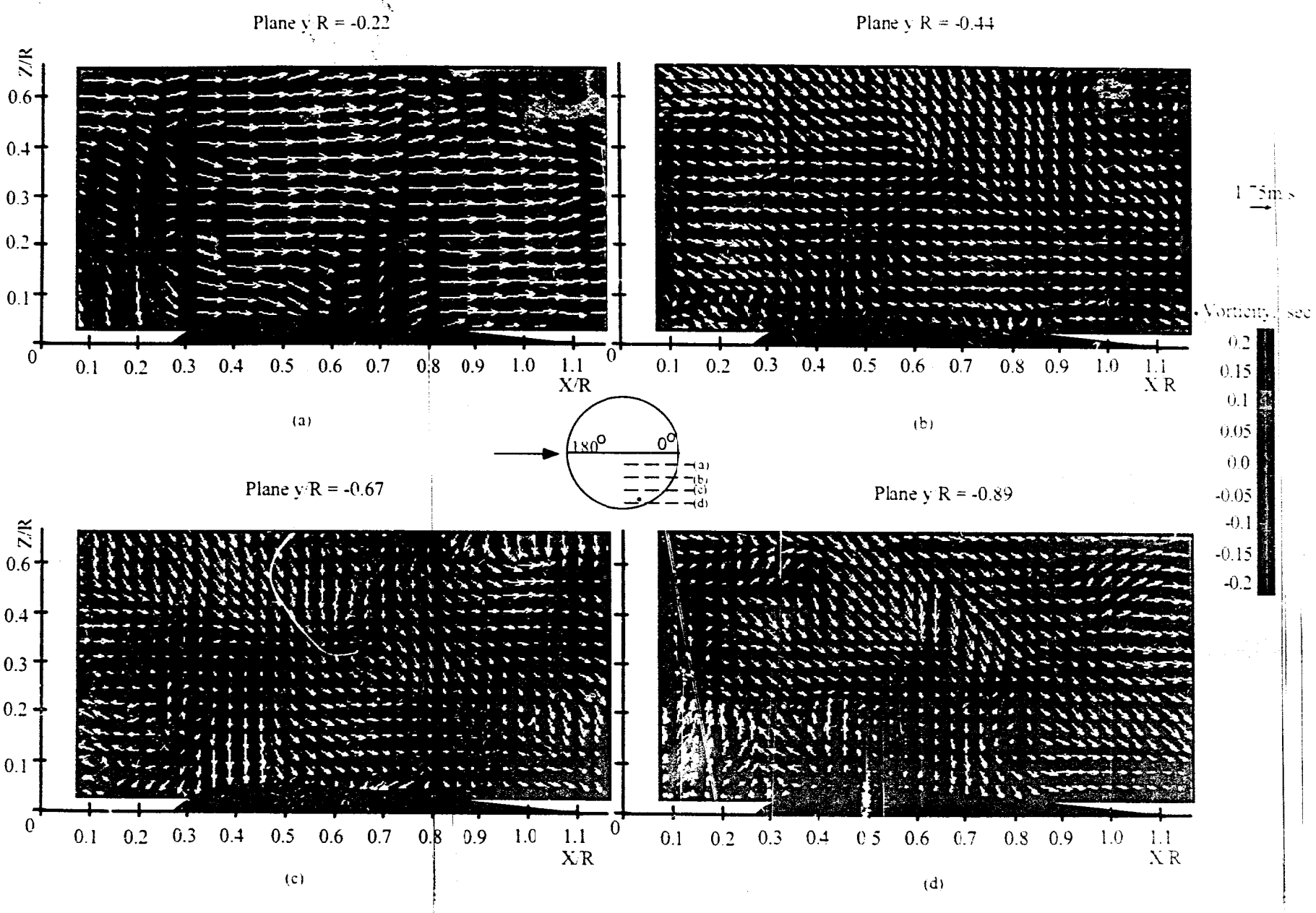

Fig. 12. Velocity vectors and vorticity contours for chordwise planes on the RBS, Ψ ~ 324